

How Good Can 2D Excitonic Solar Cells Be?

Zekun Hu,¹ Da Lin,² Jason Lynch,¹ Kevin Xu,¹ Deep Jariwala^{1,*}

¹*Department of Electrical and Systems Engineering, University of Pennsylvania, Philadelphia, PA,*

19104, USA

²*Department of Materials Science and Engineering, University of Pennsylvania, Philadelphia, PA,*

19104, USA

*Corresponding Author (D.J.) email: dmj@seas.upenn.edu

Abstract

Excitonic semiconductors have been a subject of research for photovoltaic applications for many decades. Among them, the organic polymers and small molecules based solar cells have now exceeded 19% power conversion efficiency (PCE). While organic photovoltaics (OPVs) are approaching maturity, the advent of strongly excitonic inorganic semiconductors such as two-dimensional transition metal dichalcogenides (TMDCs) has renewed interest in excitonic solar cells due to their high-optical constants, stable inorganic structure and sub-nm film thicknesses. While several reports have been published on TMDC based PVs, achieving power conversion efficiencies higher than 6% under one-sun AM1.5G illumination has remained challenging. Here, we perform a full optical and electronic analysis of design, structure and performance of monolayer TMDC based, single-junction excitonic PVs. Our computational model with optimized properties predicts a PCE of 9.22% in a superlattice device structure. Our analysis suggests that, while the PCE for 2D excitonic solar cells may be limited to < 10%, a specific power > 100 W g⁻¹ may be achieved with our proposed designs, making them attractive in aerospace, distributed remote sensing, and wearable electronics.

Introduction

Thin-film photovoltaics, such as those based on III-V semiconductors, CdTe, and 3D perovskites, have been a source of sustained research and commercial interest. However, they occupy a small share of the large-scale, grid-tied market since their production has not been scaled. Hence, their price of electricity remains high compared to silicon photovoltaics (PVs) which is the dominant PV technology¹. However, thin-film

photovoltaics have long been considered as a potential solution for lightweight applications, such as aerospace, powering distributed remote sensors, and wearable electronics^{2, 3}. In this application, new and emerging materials such as organic semiconductors⁴, II-chalcogenides⁵ and two-dimensional hybrid organic-inorganic perovskites⁶ are also being heavily investigated. Among novel, thin-film photovoltaic materials, excitonic semiconductors have attracted a lot of attention due to their large absorption coefficients which permit a sharp reduction in active layer thickness of the PV devices. However, 2D transition metal dichalcogenides (TMDCs) of MX_2 (M=Mo, W and X=S, Se, Te) have recently gained traction for lightweight PV applications. In particular, their large optical constants result in large loss-tangent values across the visible region combined with their availability in high optical and electronic quality over wafer scales makes them increasingly viable candidates for thin-film, ultralight-weight PVs^{7, 8}.

Further, a notable feature of 2D TMDC semiconductors is a transition from an indirect bandgap in bulk to the direct bandgap in monolayers that enables a high photoluminescence quantum yield, and thus, a high radiative efficiency⁹. Finally, the wide range of bandgaps (1.0-2.5 eV¹⁰) and van der Waals bonding for facile hetero-integration make TMDCs attractive candidates for single-junction, tandem, and multi-junction solar cells¹¹.

Consequently, several studies reporting microscale PV devices from bulk and monolayer TMDCs are available. However, the PCE values of these experimentally reported TMDC solar cells are typically lower than 2%¹²⁻¹⁴, whereas the highest PCEs were reported as 9.03% in MoS_2 ¹⁵ and 6.3% in WS_2 ¹⁶. Per the detailed balance model¹¹, thin-film, single-junction TMDC solar cells can have maximum PCEs of up to 27%, comparable to crystalline Silicon. This vast disparity between theoretical maximum and experimentally observed values therefore merits further investigation. To investigate the practically limiting parameters of current TMDC PVs, we developed a combined optical and electronic model to simulate the photovoltaic characteristics of four TMDC materials (MoS_2 , WS_2 , MoSe_2 , and WSe_2) based on an experimentally reported, large area, scalable superlattice structure¹⁷. Based on our model, we optimized the parameters and performance of monolayer MoS_2 superlattice based PV devices, attaining a PCE as high as 9.22% under one-sun (AM1.5) illumination with specific power exceeding 50 W/g. Finally, we benchmarked our results against other 2D PV devices on the metrics of PCE vs specific power and find that 2D TMDC based PVs when optimized for both optical and electronic design can outperform all available technologies in high specific power applications.

Results and Discussion

Device Structure and Optimization of Photon Absorption:

The proposed 2D TMDC-based photovoltaic superlattice device is shown in Figure 1a. The device consists of a repeating unit cell of a monolayer MoS₂ absorber (0.65 nm) and an Al₂O₃ insulator (3nm), and is placed on top of an Al₂O₃/Au substrate with the Au serving as a reflector. The thickness of the Al₂O₃ layer has been optimized to enhance photocarrier generation. The active layer of the device is intrinsic (no doping) which is 1 μm long, with silver and gold cathode and anode electrodes measuring 0.01 μm in length each. The heavily doped p-region (10¹⁹ cm⁻³) near the cathode and the heavily doped n-region (10¹⁹ cm⁻³) near the anode are also 0.01 μm in length. The incident angle of the light is zero, meaning it is normal to the surface. Additional details regarding the device structure and parameters used for simulation are provided in methods and in supporting information Table S1.

By using the Transfer Matrix Method (TMM) to calculate the absorbed photon density of each layer, we find that increasing the number of layers significantly increases the absorbed photon density in the 400-700 nm wavelength range as seen in Figure 1c. This increase is particularly significant when going from N=1 to N=5. However, further increasing the number of layers from N=5 to N=10 does not lead to as dramatic an increase in broadband absorptance and actually decreases the absorbed energy per unit weight. Therefore, the electrical simulations for our proposed device were based on an N=5 superlattice design. The energy band diagram for the active layer, which has a 1.80 eV bandgap for monolayer MoS₂¹⁸, is shown in Figure 1d. The band diagram is that of a p-i-n lateral homojunction takes into account the built-in field created by degenerate p-doping and n-doping near the contacts which promotes charge carrier selectivity and improves device performance¹⁹.

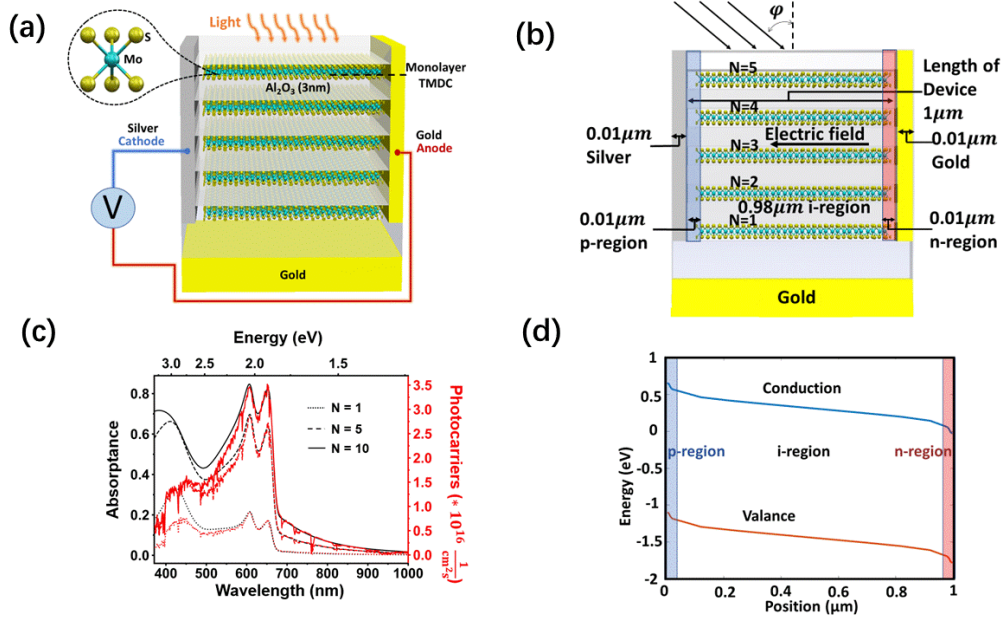


Figure 1. (a) Schematic model of the superlattice structure. (b) Side view of the model with labeled p-i-n regions and layers. (c) Simulated absorbance spectra and absorbed photon density for MoS₂/Al₂O₃ (N=1,5,10). (d) Energy band diagram of the monolayer MoS₂ for p-i-n junction.

Role of Excitons and their Radiative Efficiency

It is well known that excitons dominate the optical response of semiconducting 2D TMDCs, not only in the monolayer limit but also in the bulk. However, thus far, all attempts in literature to quantify and estimate theoretical PV potential for TMDCs have failed to treat excitons seriously in their models²⁰⁻²². Not only do excitons dominate the optical properties in low dimensional semiconductors but it is also well-known through both theory and experiment that they limit the performance of other well-known excitonic semiconductors-based PVs, namely OPVs²³⁻²⁸. Therefore, any attempt to seriously quantify the performance limits of semiconducting 2D TMDC based PVs must include a detailed treatment of excitons. In this work, we have thus examined the effects of exciton binding energy (BE), exciton radiative lifetime ($\tau_{\text{ex-r}}$), exciton nonradiative lifetime ($\tau_{\text{ex-nr}}$), and exciton diffusion length (EDL) in our model for determining performance limits of semiconducting 2D TMDC based PVs. The binding energy of excitons, which describes the ease with which an electron and hole can be separated, is important for solar cell performance. In MoS₂, the exciton binding energy increases from 0.08 eV²⁹ in the bulk to 0.44 eV³⁰ in monolayers due to quantum confinement effects³¹. However, the binding energy in monolayer TMDCs can be modified by molecular coverage³², doping³³, and engineering of the dielectric environment³⁴. By simulating the PCE as a function of exciton binding energy and diffusion length (Figure 2a and Table S2), we found that higher PCE was observed at

lower binding energies. This is because excitons are more likely to dissociate at the interface with the aid of thermal energy as the binding energy decreases (Figure S1a,b).

EDL is another crucial parameter that influences the transportation of excitons in monolayer TMDCs and therefore affects solar cell performance. Since excitons are neutral, they are not significantly affected by electric field drift. In organic solar cells, the diffusion length is on the nanometer scale, making it unlikely for an exciton to reach an electrode³⁵. In contrast, the diffusion length of TMDCs is in the micron range, allowing the electrodes to be further apart and reducing the amount of reflected light. The simulated range of 0.015-6 μm encompasses previously measured diffusion lengths in MoS_2 ³⁶. Assuming that excitons follow a Gaussian distribution centered around the diffusion length and are excited evenly throughout the MoS_2 , photocurrent is still produced even when the diffusion length is less than the distance between electrodes (1 μm). However, some excitons will still recombine before being converted into photocurrent. In silicon PVs, the recombination process releases heat due to the indirect band gap, but in our solar cell design with a direct band gap, a photon is emitted during recombination instead of heat, which does not reduce overall efficiency. The emitted photon may either be radiated out of the solar cell or reabsorbed. We did not consider the effects of reabsorption³⁷ due to our expectation that they would be low. In the blue curve of Figure 2b (0.4 eV binding energy), the PCE increases with diffusion length from 0.015 μm to 2 μm as a longer diffusion length increases the probability of an exciton reaching one of the interfaces of the junction. However, when the diffusion length becomes larger than twice the device length, nearly all the excitons reach the interfaces and begin to concentrate at the electrodes, blocking other excitons from disassociating at the interface and decreasing the PCE. For large binding energies (BE > 0.3 eV), the results for PCE, short-circuit current (I_{sc}), and open-circuit voltage (V_{oc}) were similar to the blue curve as shown in Figure S1c-e. For the red curve with a relatively low binding energy of 0.2 eV, the higher number of dissociated charges almost fully occupy the space between electrodes, resulting in a decrease in PCE as the diffusion length increases. Further increase of diffusion length results in a purely declining trend of PCE for all binding energies < 0.3 eV.

To understand the factors influencing exciton diffusion, we examined the radiative lifetime and nonradiative lifetime of the excitons based on a binding energy of 0.24 eV³⁸ and a diffusion length of 1.5 μm . The quantum yield of monolayer MoS_2 can range from less than 1% to nearly 100%, and the effective lifetime can be as long as 10 ns³⁹. We first conducted simulations varying the exciton radiative lifetime from 0.0001-10 ns and the exciton nonradiative lifetime from 0.0001-10 ns, which modified the quantum yield from less than 1% to greater than 99% (Figure 2c and Figure S2a,b). Previous reports have also found radiative lifetimes ranging from 0.2 ps⁴⁰ to 15 ns⁴¹ and nonradiative lifetimes from 1 ps to 10 ps⁴² in MoS_2 . In order to more closely examine the effect of these lifetimes on PCE, we further studied the range with logarithmic axes in Figure 2d and Figure S2c,d. As the simulations did not take into account the reabsorption of photons from recombination, the quantum yield had no impact on PCE.

The total lifetime, which is the combination of radiative and nonradiative lifetimes, determines the photocurrent and PCE. A longer lifetime means excitons exist longer before recombining and have a higher chance of diffusing and dissociating, leading to higher photocurrent from an increase in charges. In Figure 2d, improving the nonradiative lifetime is more important than improving the radiative lifetime as defects significantly trap the excitons and reduce the total lifetime, and therefore the efficiency of the photovoltaic device. In the optimization process, we selected 10 ns for both radiative and nonradiative lifetimes, resulting in a PCE of 5.62%.

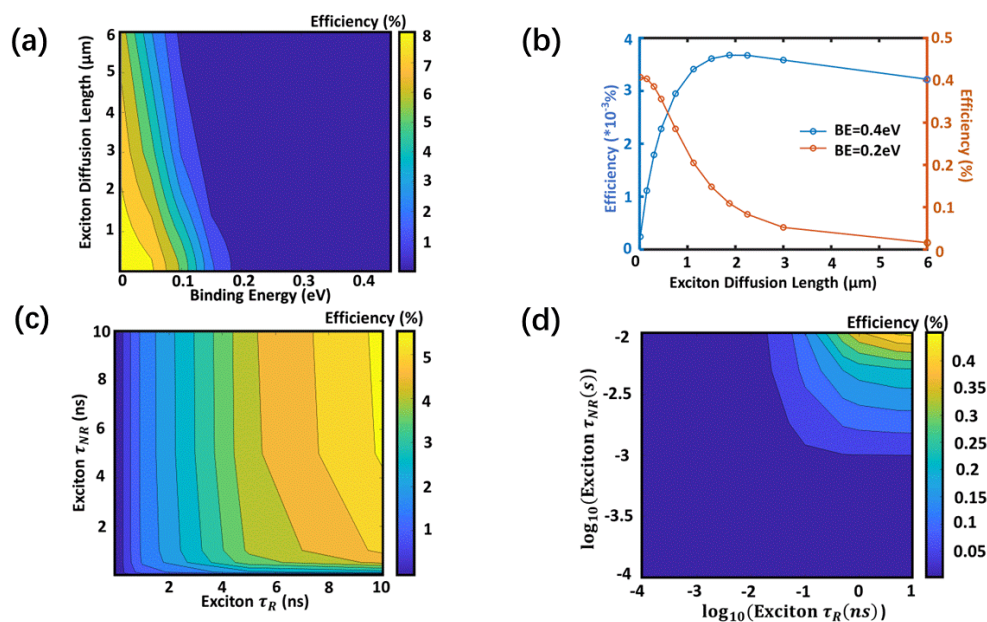


Figure 2. (a) The PCE for the variation of exciton binding energy (0-0.5 eV) and diffusion length (0.015-6 μm). (b) The PCE for the variation of exciton diffusion length for BE=0.2 eV, 0.4 eV. (c) The PCE for the variation of $\tau_{\text{ex-r}}$ and $\tau_{\text{ex-nr}}$ (0.0001-10 ns). (d) The current density for the variation of $\tau_{\text{ex-r}}$ (0.0001-0.01 ns) and $\tau_{\text{ex-nr}}$ (0.0001-10 ns).

Role of free carriers and their mobilities

After optimizing the parameters of exciton binding energy and exciton lifetimes, we examined the effect of free carrier properties under an electric field on photocurrent. The electron mobility of monolayer MoS₂ has been reported to be in the range of 0.1-10 $\text{cm}^2\text{V}^{-1}\text{s}^{-1}$ ^{43, 44}. However, the carrier mobility can be improved using the dielectric screening effect⁴⁵, allowing for values greater than 100 $\text{cm}^2\text{V}^{-1}\text{s}^{-1}$ ^{46, 47}. We therefore studied the range of free carrier mobilities from 0.1 to 200 $\text{cm}^2\text{V}^{-1}\text{s}^{-1}$ and device lengths from 0.4 to 10 μm (Figure 3a and Figure S3). As the electron mobility increases, the PCE is enhanced as more photocarriers are collected by the electrodes. In Figure 3b, we see that the PCE increases significantly in the mobility range of 0.1-60 $\text{cm}^2\text{V}^{-1}\text{s}^{-1}$ for several selected device lengths (0.4, 0.6, 1, 2, and 3 μm). The largest enhancement in PCE is seen when the free carrier mobility is increased to 100 $\text{cm}^2\text{V}^{-1}\text{s}^{-1}$ and the

radiative lifetime to 6 ns, values that can be achieved in MoS₂ without additional treatments or dielectric engineering.

To understand the impact of electron mobility, we also analyzed the effect of device length. In Figure 3a and Figure S3a,b, we see that the peak PCE occurs at a device length around 1 μm . A similar result is also seen in Figure 3c and Figure S3c,d, where the exciton total lifetime is varied from 0.01 to 6 ns. As these simulations are based on a constant exciton diffusion length of 1.5 μm (other parameters are in Table S4), the optimized device length is comparable to the exciton diffusion length. For lengths greater than 1 μm , the portion of excitons in the i-region diffusing to the dissociation region decreases, leading to a decrease in PCE. For lengths shorter than 1 μm , the exciton diffusion length of 1.5 μm exceeds the dissociation region, also leading to a decrease in PCE. In Figure 3c, we see that increasing the exciton total lifetime significantly increases photocurrent and PCE. In addition to carrier mobility, we also studied the carrier lifetime over the range of 0.5 to 10 ns, where the dominant recombination process at low carrier concentrations is Shockley-Read-Hall (SRH) recombination⁴⁸. In Figure 3d, we see that the PCE increases nonlinearly with carrier lifetime. For SRH lifetimes shorter than 3 ns, the significant increase in PCE shows that the carrier lifetime is a limiting factor for final efficiency. However, for SRH lifetimes longer than 3 ns, the slow increase in PCE indicates that the SRH lifetime is no longer a limiting factor.

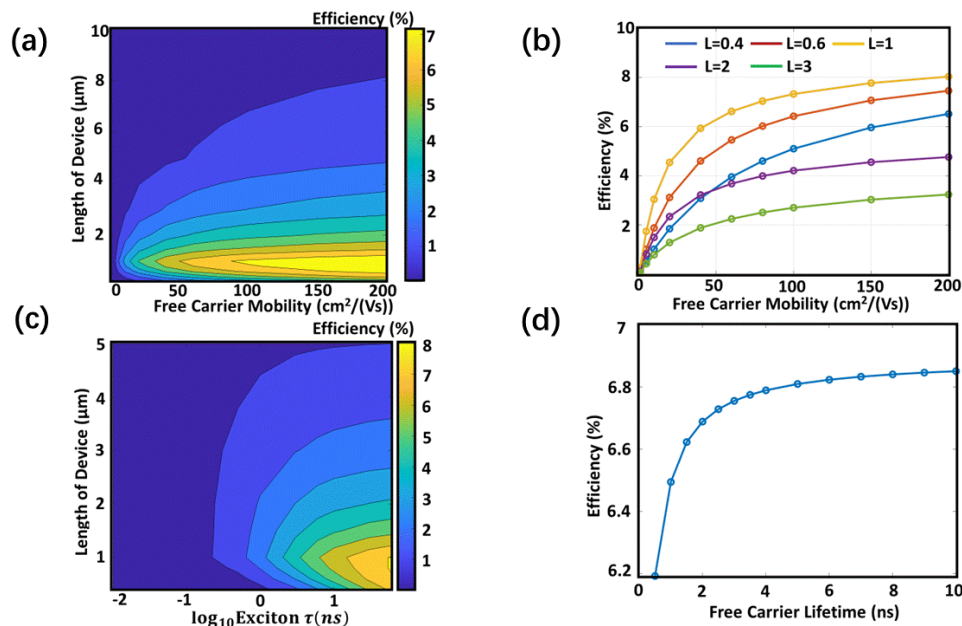


Figure 3. (a) The PCE for the variation of length of device (0.4-10 μm) and free carrier mobility (0.1-200 $\text{cm}^2/(\text{Vs})$) under exciton lifetime of 10 ns). (b) The PCE for the variation of free carrier mobility for length of device = 0.4 μm , 0.6 μm , 1 μm , 2 μm , 3 μm . (c) The PCE for the variation of length of device (0.2-10 μm) and exciton lifetime (0.01-6 ns) under free carrier mobility of 60 $\text{cm}^2/(\text{Vs})$). (d) The PCE for the variation of free carrier lifetime under free carrier mobility of 60 $\text{cm}^2/(\text{Vs})$.

Angle sensitivity and comparison between different TMDCs

The photocarrier generation of the superlattice for $N = 1$ to 10 with optimized bottom alumina thicknesses was investigated at different incident angles. The photocarrier generation rate was found to have a maximum in the range of 50° to 65° for all values of N . This increased rate is due to the formation of exciton-polaritons, which allows for near unity absorption of transverse electric polarized light near the photon density maximum of the AM1.5 solar spectrum. However, the absorption at other wavelengths decreases as the incident angle increases due to the initial interface becoming more reflective. The maximum occurs at lower incident angles as N increases because the increased Rabi splitting allows for the formation of exciton-polaritons at lower incident angles. Simulations of the absorbed photons at different incident angles were used to calculate the PCE as shown in Figure 4b. The peak PCE of 0.24 eV binding energy was 9.22% at an incident angle of 50° . After optimization, the internal quantum efficiency (IQE) reached a maximum of 69.5%. The IQE did not change when the incident angle was varied in the simulation using the angle dependent photon absorption spectra, which explained the same curvature seen in Figure 4a ($N=5$) and 4b. The final PCE is proportional to absorbed photons for a constant IQE.

The performance of superlattices made from four different TMDCs, MoS₂, MoSe₂, WS₂, and WSe₂, was also simulated using our model. The absorbed photon density was calculated using TMM simulations, as shown in Table 1. Figure 4c shows the absorbed photon density and the PCEs of different material. MoS₂ had the largest photon absorption density and the highest PCE due to its two lowest energy excitons being near the maximum of the solar photon spectrum and its relatively low binding energy of 0.24 eV, which resulted in an IQE of 56.72%. MoSe₂ had a higher binding energy of 0.57 eV, leading to a significantly lower IQE of 3.79% and a PCE of 0.06%. WS₂ had a relatively high free carrier mobility of $1000 \text{ cm}^2\text{V}^{-1}\text{s}^{-1}$ and a low binding energy of 0.32 eV, resulting in the highest IQE of 81.24%. However, its relatively lower photon absorption rate led to a final PCE of 1.98%. WSe₂ had a relatively low photon absorption rate and a high binding energy of 0.37 eV, resulting in a PCE of 0.36%. These results show that reducing the exciton binding energy is crucial for producing high-efficiency solar cells using this geometry. The actual binding energy of excitons in the superlattice is expected to be lower by a factor of approximately 2 due to the use of binding energy values for freestanding samples. The binding energy can be further reduced by using high refractive index spacer layers such as hBN, TiO₂, and Ta₂O₅. Figure 4d shows the current-voltage (I-V) curves of the four materials. In this comparison, MoS₂ had the best short-circuit current density of the four TMDCs studied, while WS₂ had the largest open-circuit voltage and fill factor (FF).

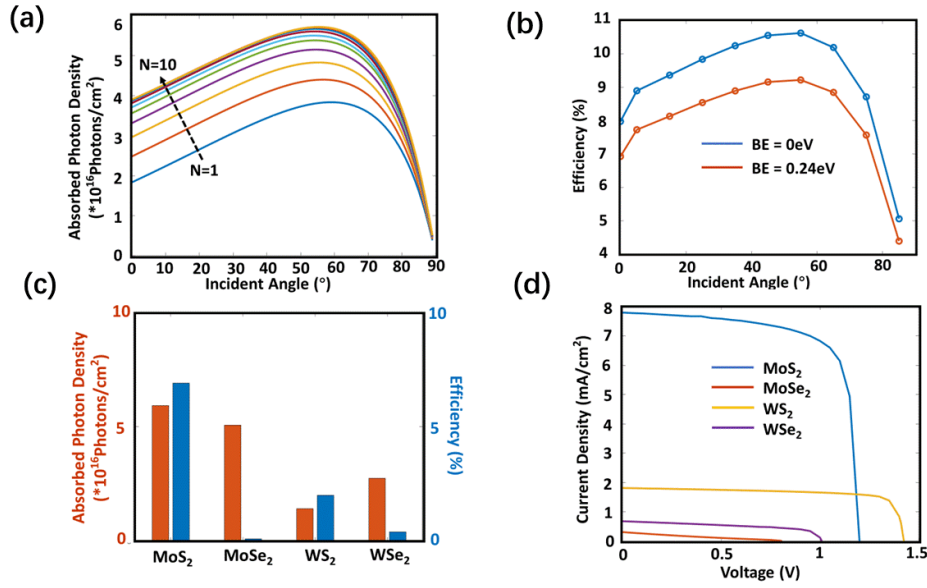


Figure 4. (a) The absorbed photon density for the different incident angle (0-90°) and different layers (N=1-10). (b) The PCE for the variation of the incident angle (0-90°) for binding energy = 0eV, 0.24eV. (c) The absorbed photon density and PCE for MoS₂, MoSe₂, WS₂, and WSe₂. (d) The I-V curve for MoS₂, MoSe₂, WS₂, and WSe₂.

Table 1. The key parameters of TMDC materials (MoS₂, MoSe₂, WS₂, WSe₂).

	MoS ₂	MoSe ₂	WS ₂	WSe ₂
Absorbed photons ($\times 10^{16}$ photons/cm²)	5.94404	5.07596	1.39183	2.72686
Bandgap (eV)	1.8¹⁸	1.60⁴⁹	2.04⁵⁰	1.65⁴⁹
Binding Energy (eV)	0.24³⁸	0.57⁵¹	0.32³⁰	0.37⁴⁹
Mobility (cm²/V/s)	60⁵²	480⁵³	1060⁵⁴	250⁵⁵
Short Circuit Current (mA/cm²)	5.40	0.31	1.81	0.68
Open Circuit Voltage (V)	1.20	0.82	1.42	1.01
Fill Factor	70.15	22.36	76.58	53.21
Internal Quantum Efficiency (%)	56.72	3.79	81.24	15.54
Power Conversion Efficiency (%)	4.54	0.06	1.98	0.36

At a PCE of 9.22% and a specific weight of 0.58 g m^{-2} , excluding a supporting substrate, our device has a specific power (power/weight ratio) of 157 W g^{-1} , which is the highest value among TMDC-based cells to the best of our knowledge. We compared the PCE performance and power/weight ratio of our modelled device to other TMDC containing photovoltaic devices from recent literature under AM1.5 illumination (Figure 5)^{12-14, 56-70}. Further details on the calculation of specific power for each cell are provided in the Methods section. We found that our solar cell had the largest specific power of all TMDC-based solar cells to the best of our knowledge. This is because previous TMDC-based solar cells have either used monolayer samples for their ideal electronic properties at the expense of lower absorption, or they have used thin films, typically $>100 \text{ nm}$, which has large absorption while increasing the weight. However, our design achieves large absorption while also having the advantage of the lightweight, high electrical quality of monolayer TMDCs.

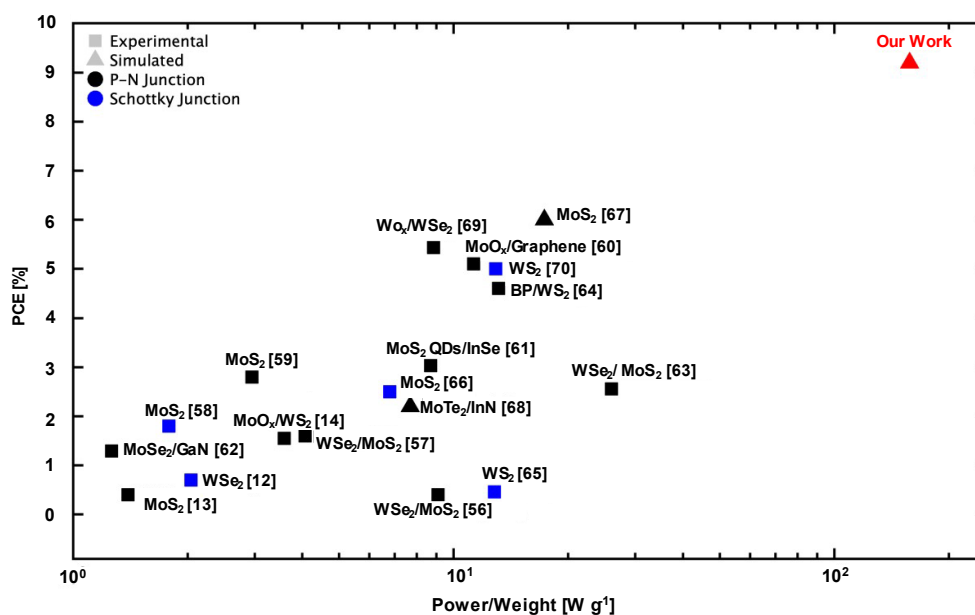


Figure 5. Efficiency chart of vdW material-based photovoltaic with their power/weight ratio in unit of W g^{-1} .

We also compared our solar cell to the highest specific power that has been achieved in other materials⁷¹⁻⁷⁵ (Figure 6). Although our solar cell has the lowest PCE of all the materials at 9.2% where the rest of the materials range from 11.2% to 22.35%, our exceptionally small active layer thickness of 3.5 nm results in TMDCs having the highest potential specific powers of all of the materials. Since our TMDC-based solar cell has the largest PCE, along with its simplicity and ease of large-scale fabrication, it can be a great candidate for lightweight solar cells in fields such as space, aerospace as well as wearable electronics and remote sensors.

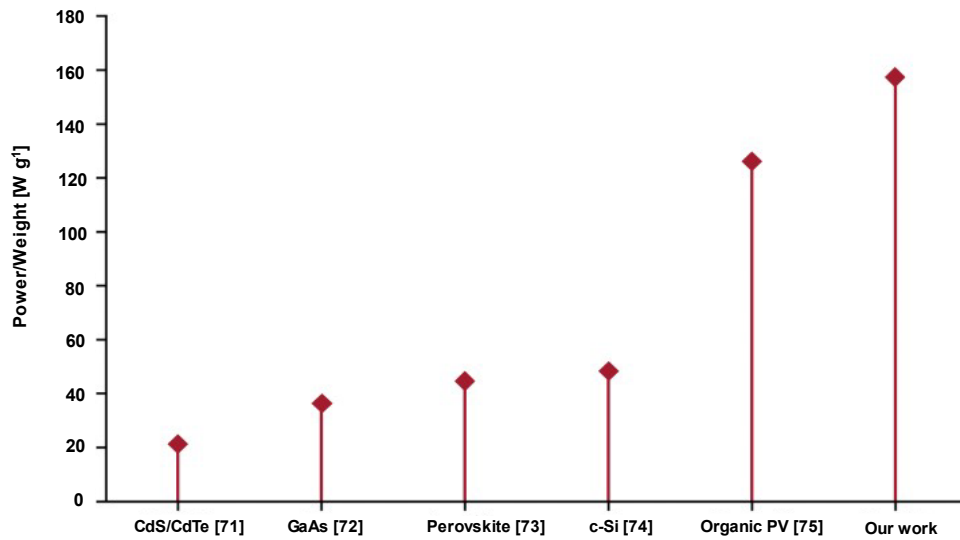


Figure 6. Power/weight ratio chart of different lightweight PV technologies in unit of $W g^{-1}$.

Conclusion

In summary, we have proposed a device structure and model for 2D TMDC based excitonic solar cells and provided a thorough investigation of the physical factors limiting their performance. The principal innovation of our work lies in the optimization of both the optical and electronic properties and accounting for excitonic effects to estimate the highest possible PCE values using practical materials and device parameters. Our findings suggest that the large exciton binding energies limit the overall efficiencies of 2D TMDC based PV devices to about a third of those predicted by the detailed balance model. None the less, even with large exciton binding energies upon optimizing various geometric and materials quality parameters, a PCE of 9.22% was achieved for MoS₂. Even with these PCE values, the total active layer thickness of our proposed optimized device structures is < 4 nm making them some of the highest specific power cells ($> 100 W g^{-1}$) of any thin-film PV technology available today. Overall, our work lays a firm theoretical foundation and computational model on the performance limits of 2D TMDC based excitonic solar cells.

Methods

Photocurrent Generation Calculations

The transfer matrix method⁷⁶ was implemented in python to simulate the photocurrent generation rate of the superlattice due to its ability to accurately model the absorption spectra of 1D systems. The refractive index of monolayer TMDCs, Al₂O₃, and Au were all taken from literature^{77, 78}. The photocurrent generation rate was then calculated by multiplying the absorption spectrum of the superlattice by the AM1.5 solar spectrum⁷⁹. For non-normal incidence, the absorption spectra for TE and TM light were averaged to calculate the absorption spectrum of unpolarized light.

Sentaurus Simulation

The two-dimensional solid-state p-i-n superlattice structure was numerically simulated using Sentaurus. This tool is beneficial to elucidate the solar cell behavior considering many physical mechanisms in the device (such as different recombination, different photon absorption calculation). Due to the limitation of vertices number and the long simulation time of the 3D model, a 2D simulation was adopted after we converged on parameters from the 3D model. The 2D simulation has a default thickness of 1 μm in the third dimension where the variation of thickness will not affect the result, details can be found in S3. The structure consists of the monolayer active materials (MoS₂, MoSe₂, WS₂, WSe₂), insulators (Al₂O₃), cathode (Ag), and anode (Au). The thick bottom insulator and gold bottom were not included in the Sentaurus simulation as their effects were fully considered in the photon generation simulation. The investigation of the impact of binding energy, exciton diffusion length, exciton radiative lifetime, exciton nonradiative lifetime, free carrier mobility, free carrier SRH lifetime, and device length on V_{oc}, J_{sc}, FF and PCE have been performed by utilizing this model.

The initial input parameters were obtained from the experimental data and other theoretical results to define the structure and materials as shown in Table. S1-6. In this model, the electron and hole densities were computed from the electron and hole quasi-Fermi potentials. The bandgap was based on reported values and the Bandgap narrowing effect was not considered. This model allowed discontinuous interfaces for a superlattice structure. By defining the heterointerface, the datasets of two materials were treated properly by introducing double points. The optical generation was based on our TMM results and was defined manually for each layer. The carrier recombination considered three forms, SRH, Auger and radiative. Sentaurus solved the Poisson and continuity equations to account for optical properties. The equation modeled the dynamic of the generation, diffusion, recombination, and radiative decay of singlet excitons^{80, 81}, is given by:

$$\frac{\partial n_{se}}{\partial t} = R_{bimolec} + \nabla * D_{se} \nabla n_{se} - \frac{n_{se} - n_{se}^{eq}}{\tau} - \frac{n_{se} - n_{se}^{eq}}{\tau_{trap}} - R_{se} \quad \text{Equ.1}$$

Where n_{se} is the singlet exciton density, $R_{bimolec}$ is the carrier bimolecular recombination rate acting as a singlet exciton generation term, D_{se} is the singlet exciton diffusion constant, τ , τ_{trap} are the singlet exciton lifetimes. R_{se} is the net singlet exciton recombination rate.

Specific power estimations,

In determining the power/weight ratio for the devices compared in Figure 5 and Figure 6, the specific power (W m^{-2}) and specific weight (g m^{-2}) are individually calculated. All devices evaluated presented power conversion efficiencies with the AM1.5 spectrum (integrated power = 1000 W m^{-2}), thus yielding a specific power that is the PCE fraction of the integrated spectrum power. As there lacks a unified way of calculating specific weight in TMDC photovoltaics, this work views the minimum specific weight sufficient to achieve the given PCE as the comparing metric, positioning this approach specifically as a method for comparing thin film solar cells from a practical optimization perspective. Every layer of a device that actively contributes to power conversion is included in the specific weight, including electrodes which are included based on areal coverage. For layers that do not directly contribute to power conversion but play a role in the optics of the device, such as dielectrics, metal reflectors, and oxide-coated substrates, an effective thickness is used, when smaller than the actual layer thickness, equal to light's penetration depth into the material at the peak of the AM1.5 spectrum (500 nm). Substrates that do not play a role in either the electronic or optical behavior of the device, such as polymer films added for device flexibility, are not included in specific weight calculations given that thicknesses vary across devices without uniform logic. The specific weight is found by multiplying the effective thickness of each included layer in the device by the material density, which was found in literature. Note that the full substrate thickness is used in specific device configurations, such as p-n junction cells where the substrate serves as the p/n side. Dividing specific power by specific weight thus yields the power/weight ratio (W g^{-1}).

Acknowledgements: D.J., Z. H. and J.L. acknowledge primary support for this work by the Asian Office of Aerospace Research and Development (AOARD) and the Air Force Office of Scientific Research (AFOSR) FA2386-20-1-4074 and FA2386-21-1-4063. D.J. also acknowledges partial support from the Office of Naval Research (N00014-23-1-203) University Research Foundation at Penn and the Alfred P. Sloan Foundation for the Sloan Fellowship. D. L., K. X. and D. J. acknowledges support from the Center for Undergraduate Research Fellowships (CURF) at U. Penn. All authors thank Francisco Barrera for his assistance in setting up simulations and certain material parameters.

References:

- (1) Efaz, E. T.; Rhaman, M. M.; Imam, S. A.; Bashar, K. L.; Kabir, F.; Mourtaza, M. D. E.; Sakib, S. N.; Mozahid, F. A. A review of primary technologies of thin-film solar cells. *Engineering Research Express* **2021**, *3* (3), 032001. DOI: 10.1088/2631-8695/ac2353.
- (2) Reese, M. O.; Glynn, S.; Kempe, M. D.; McGott, D. L.; Dabney, M. S.; Barnes, T. M.; Booth, S.; Feldman, D.; Haegel, N. M. Increasing markets and decreasing package weight for high-specific-power photovoltaics. *Nature Energy* **2018**, *3* (11), 1002-1012. DOI: 10.1038/s41560-018-0258-1.
- (3) Mathews, I.; Kantareddy, S. N.; Buonassisi, T.; Peters, I. M. Technology and Market Perspective for Indoor Photovoltaic Cells. *Joule* **2019**, *3* (6), 1415-1426. DOI: <https://doi.org/10.1016/j.joule.2019.03.026>.
- (4) Sampaio, P. G. V.; González, M. O. A. A review on organic photovoltaic cell. *International Journal of Energy Research* **2022**, *46* (13), 17813-17828. DOI: <https://doi.org/10.1002/er.8456>.
- (5) Li, Y.; Wang, L.; Qiao, Y.; Gan, Y.; Singh, D. J. Prediction of ternary alkaline-earth metal Sn(II) and Pb(II) chalcogenide semiconductors. *Physical Review Materials* **2020**, *4* (5), 055004. DOI: 10.1103/PhysRevMaterials.4.055004.
- (6) Hou, Y.; Wu, C.; Yang, D.; Ye, T.; Honavar, V. G.; Duin, A. C. T. v.; Wang, K.; Priya, S. Two-dimensional hybrid organic-inorganic perovskites as emergent ferroelectric materials. *Journal of Applied Physics* **2020**, *128* (6), 060906. DOI: 10.1063/5.0016010.
- (7) Kang, K.; Lee, K.-H.; Han, Y.; Gao, H.; Xie, S.; Muller, D. A.; Park, J. Layer-by-layer assembly of two-dimensional materials into wafer-scale heterostructures. *Nature* **2017**, *550* (7675), 229-233. DOI: 10.1038/nature23905.
- (8) Laturia, A.; Van de Put, M. L.; Vandenberghe, W. G. Dielectric properties of hexagonal boron nitride and transition metal dichalcogenides: from monolayer to bulk. *npj 2D Materials and Applications* **2018**, *2* (1), 6. DOI: 10.1038/s41699-018-0050-x.
- (9) Amani, M.; Lien, D.-H.; Kiriya, D.; Xiao, J.; Azcatl, A.; Noh, J.; Madhupathy, S. R.; Addou, R.; Kc, S.; Dubey, M.; et al. Near-unity photoluminescence quantum yield in MoS₂. *Science* **2015**, *350* (6264), 1065-1068. DOI: 10.1126/science.aad2114 PubMed.
- (10) Wang, L.; Huang, L.; Tan, W. C.; Feng, X.; Chen, L.; Huang, X.; Ang, K.-W. 2D Photovoltaic Devices: Progress and Prospects. *Small Methods* **2018**, *2* (3), 1700294. DOI: <https://doi.org/10.1002/smtd.201700294>.
- (11) Jariwala, D.; Davoyan, A. R.; Wong, J.; Atwater, H. A. Van der Waals Materials for Atomically-Thin Photovoltaics: Promise and Outlook. *ACS Photonics* **2017**, *4* (12), 2962-2970. DOI: 10.1021/acsp Photonics.7b01103.
- (12) Akama, T.; Okita, W.; Nagai, R.; Li, C.; Kaneko, T.; Kato, T. Schottky solar cell using few-layered transition metal dichalcogenides toward large-scale fabrication of semitransparent and flexible power generator. *Sci Rep* **2017**, *7* (1), 11967. DOI: 10.1038/s41598-017-12287-6 From NLM PubMed-not-MEDLINE.
- (13) Li, H. M.; Lee, D.; Qu, D.; Liu, X.; Ryu, J.; Seabaugh, A.; Yoo, W. J. Ultimate thin vertical p-n junction composed of two-dimensional layered molybdenum disulfide. *Nat Commun* **2015**, *6*, 6564. DOI: 10.1038/ncomms7564 From NLM PubMed-not-MEDLINE.
- (14) Nassiri Nazif, K.; Kumar, A.; Hong, J.; Lee, N.; Islam, R.; McClellan, C. J.; Karni, O.; van de Groep,

- J.; Heinz, T. F.; Pop, E.; et al. High-Performance p-n Junction Transition Metal Dichalcogenide Photovoltaic Cells Enabled by MoO_x Doping and Passivation. *Nano Lett* **2021**, *21* (8), 3443–3450. DOI: 10.1021/acs.nanolett.1c00015 From NLM PubMed-not-MEDLINE.
- (15) Lin, S.; Li, X.; Wang, P.; Xu, Z.; Zhang, S.; Zhong, H.; Wu, Z.; Xu, W.; Chen, H. Interface designed MoS₂/GaAs heterostructure solar cell with sandwich stacked hexagonal boron nitride. *Scientific Reports* **2015**, *5* (1), 15103. DOI: 10.1038/srep15103.
- (16) Hussain, S.; Shaikh, S. F.; Vikraman, D.; Mane, R. S.; Joo, O.-S.; Naushad, M.; Jung, J. Sputtering and sulfurization-combined synthesis of a transparent WS₂ counter electrode and its application to dye-sensitized solar cells. *RSC Advances* **2015**, *5* (125), 103567–103572, 10.1039/C5RA18613G. DOI: 10.1039/C5RA18613G.
- (17) Kumar, P.; Lynch, J.; Song, B.; Ling, H.; Barrera, F.; Kisslinger, K.; Zhang, H.; Anantharaman, S. B.; Digani, J.; Zhu, H.; et al. Light-matter coupling in large-area van der Waals superlattices. *Nat Nanotechnol* **2022**, *17* (2), 182–189. DOI: 10.1038/s41565-021-01023-x From NLM PubMed-not-MEDLINE.
- (18) Castellanos-Gomez, A.; Barkelid, M.; Goossens, A. M.; Calado, V. E.; van der Zant, H. S.; Steele, G. A. Laser-thinning of MoS₂: on demand generation of a single-layer semiconductor. *Nano Lett* **2012**, *12* (6), 3187–3192. DOI: 10.1021/nl301164v From NLM Medline.
- (19) Cai, L.; McClellan, C. J.; Koh, A. L.; Li, H.; Yalon, E.; Pop, E.; Zheng, X. Rapid Flame Synthesis of Atomically Thin MoO₃ down to Monolayer Thickness for Effective Hole Doping of WSe₂. *Nano Letters* **2017**, *17* (6), 3854–3861. DOI: 10.1021/acs.nanolett.7b01322.
- (20) Roy, S.; Bermel, P. Tungsten-Disulfide-Based Ultrathin Solar Cells for Space Applications. *IEEE Journal of Photovoltaics* **2022**, *12* (5), 1184–1191. DOI: 10.1109/JPHOTOV.2022.3179986.
- (21) Roy, S.; Hu, Z.; Kais, S.; Bermel, P. Enhancement of Photovoltaic Current through Dark States in Donor-Acceptor Pairs of Tungsten-Based Transition Metal Di-Chalcogenides. *Advanced Functional Materials* **2021**, *31* (23), 2100387. DOI: <https://doi.org/10.1002/adfm.202100387>.
- (22) Khan, M. A. U.; Adesina, N. O.; Xu, J. Near Unity Absorbance and Photovoltaic Properties of TMDC/Gold Heterojunction for Solar Cell Application. *Key Engineering Materials* **2022**, *918*, 97–105. DOI: 10.4028/p-uz62m4.
- (23) Classen, A.; Chochos, C. L.; Lüer, L.; Gregoriou, V. G.; Wortmann, J.; Osvet, A.; Forberich, K.; McCulloch, I.; Heumüller, T.; Brabec, C. J. The role of exciton lifetime for charge generation in organic solar cells at negligible energy-level offsets. *Nature Energy* **2020**, *5* (9), 711–719. DOI: 10.1038/s41560-020-00684-7.
- (24) Kirchartz, T.; Rau, U. Charge separation in excitonic and bipolar solar cells — A detailed balance approach. *Thin Solid Films* **2008**, *516* (20), 7144–7148. DOI: <https://doi.org/10.1016/j.tsf.2007.12.084>.
- (25) Kirchartz, T.; Mattheis, J.; Rau, U. Detailed balance theory of excitonic and bulk heterojunction solar cells. *Physical Review B* **2008**, *78* (23), 235320. DOI: 10.1103/PhysRevB.78.235320.
- (26) Bisquert, J.; Garcia-Belmonte, G. On Voltage, Photovoltage, and Photocurrent in Bulk Heterojunction Organic Solar Cells. *The Journal of Physical Chemistry Letters* **2011**, *2* (15), 1950–1964. DOI: 10.1021/jz2004864.
- (27) Bisquert, J. *The physics of solar cells: perovskites, organics, and photovoltaic fundamentals*; CRC press, 2017.
- (28) Savoie, B. M.; Rao, A.; Bakulin, A. A.; Gelinias, S.; Movaghar, B.; Friend, R. H.; Marks, T. J.; Ratner, M. A. Unequal Partnership: Asymmetric Roles of Polymeric Donor and Fullerene Acceptor in

Generating Free Charge. *Journal of the American Chemical Society* **2014**, *136*(7), 2876-2884. DOI: 10.1021/ja411859m.

(29) Saigal, N.; Sugunakar, V.; Ghosh, S. Exciton binding energy in bulk MoS₂: A reassessment. *Applied Physics Letters* **2016**, *108*(13), 132105. DOI: 10.1063/1.4945047.

(30) Hill, H. M.; Rigosi, A. F.; Roquelet, C.; Chernikov, A.; Berkelbach, T. C.; Reichman, D. R.; Hybertsen, M. S.; Brus, L. E.; Heinz, T. F. Observation of Excitonic Rydberg States in Monolayer MoS₂ and WS₂ by Photoluminescence Excitation Spectroscopy. *Nano Letters* **2015**, *15*(5), 2992-2997. DOI: 10.1021/nl504868p.

(31) Bryant, G. W. Excitons in quantum boxes: Correlation effects and quantum confinement. *Physical Review B* **1988**, *37*(15), 8763-8772. DOI: 10.1103/PhysRevB.37.8763.

(32) Wang, K.; Paulus, B. Tuning the binding energy of excitons in the MoS₂ monolayer by molecular functionalization and defective engineering. *Phys Chem Chem Phys* **2020**, *22*(21), 11936-11942. DOI: 10.1039/d0cp01239d From NLM PubMed-not-MEDLINE.

(33) Li, Z.; Xiao, Y.; Gong, Y.; Wang, Z.; Kang, Y.; Zu, S.; Ajayan, P. M.; Nordlander, P.; Fang, Z. Active Light Control of the MoS₂ Monolayer Exciton Binding Energy. *ACS Nano* **2015**, *9*(10), 10158-10164. DOI: 10.1021/acs.nano.5b03764.

(34) Raja, A.; Chaves, A.; Yu, J.; Arefe, G.; Hill, H. M.; Rigosi, A. F.; Berkelbach, T. C.; Nagler, P.; Schüller, C.; Korn, T.; et al. Coulomb engineering of the bandgap and excitons in two-dimensional materials. *Nature Communications* **2017**, *8*(1), 15251. DOI: 10.1038/ncomms15251.

(35) Luhman, W. A.; Holmes, R. J. Investigation of Energy Transfer in Organic Photovoltaic Cells and Impact on Exciton Diffusion Length Measurements. *Advanced Functional Materials* **2011**, *21*(4), 764-771. DOI: <https://doi.org/10.1002/adfm.201001928>.

(36) Uddin, S. Z.; Kim, H.; Lorenzon, M.; Yeh, M.; Lien, D. H.; Barnard, E. S.; Htoon, H.; Weber-Bargioni, A.; Javey, A. Neutral Exciton Diffusion in Monolayer MoS₂. *ACS Nano* **2020**, *14*(10), 13433-13440. DOI: 10.1021/acs.nano.0c05305 From NLM PubMed-not-MEDLINE.

(37) Yamada, T.; Yamada, Y.; Nakaike, Y.; Wakamiya, A.; Kanemitsu, Y. Photon Emission and Reabsorption Processes in $\text{CH}_3\text{NH}_3\text{PbBr}_3$ Single Crystals Revealed by Time-Resolved Two-Photon-Excitation Photoluminescence Microscopy. *Physical Review Applied* **2017**, *7*(1), 014001. DOI: 10.1103/PhysRevApplied.7.014001.

(38) Park, S.; Mutz, N.; Schultz, T.; Blumstengel, S.; Han, A.; Aljarb, A.; Li, L.-J.; List-Kratochvil, E. J. W.; Amsalem, P.; Koch, N. Direct determination of monolayer MoS₂ and WSe₂ exciton binding energies on insulating and metallic substrates. *2D Materials* **2018**, *5*(2), 025003. DOI: 10.1088/2053-1583/aaa4ca.

(39) Lien, D.-H.; Uddin, S. Z.; Yeh, M.; Amani, M.; Kim, H.; Ager, J. W.; Yablonovitch, E.; Javey, A. Electrical suppression of all nonradiative recombination pathways in monolayer semiconductors. *Science* **2019**, *364*(6439), 468-471. DOI: doi:10.1126/science.aaw8053.

(40) Wang, H.; Zhang, C.; Chan, W.; Manolatu, C.; Tiwari, S.; Rana, F. Radiative lifetimes of excitons and trions in monolayers of the metal dichalcogenide MoS₂. *Physical Review B* **2016**, *93*(4). DOI: 10.1103/PhysRevB.93.045407.

(41) Kim, H.; Lien, D.-H.; Amani, M.; Ager, J. W.; Javey, A. Highly Stable Near-Unity Photoluminescence Yield in Monolayer MoS₂ by Fluoropolymer Encapsulation and Superacid Treatment. *ACS Nano* **2017**, *11*(5), 5179-5185. DOI: 10.1021/acs.nano.7b02521.

(42) Palummo, M.; Bernardi, M.; Grossman, J. C. Exciton radiative lifetimes in two-dimensional transition metal dichalcogenides. *Nano Lett* **2015**, *15*(5), 2794-2800. DOI: 10.1021/nl503799t

From NLM Medline.

(43) Kim, T.; Fan, S.; Lee, S.; Joo, M. K.; Lee, Y. H. High-mobility junction field-effect transistor via graphene/MoS₂ heterointerface. *Sci Rep* **2020**, *10*(1), 13101. DOI: 10.1038/s41598-020-70038-6
From NLM PubMed-not-MEDLINE.

(44) Liu, H.; Neal, A. T.; Ye, P. D. Channel Length Scaling of MoS₂ MOSFETs. *ACS Nano* **2012**, *6*(10), 8563-8569. DOI: 10.1021/nn303513c.

(45) Rai, A.; Valsaraj, A.; Mowva, H. C. P.; Roy, A.; Tutuc, E.; Register, L. F.; Banerjee, S. K. Interfacial-oxygen-vacancy mediated doping of MoS₂ by high- κ dielectrics. In *2015 73rd Annual Device Research Conference (DRC)*, 21-24 June 2015, 2015; pp 189-190. DOI: 10.1109/DRC.2015.7175626.

(46) Choi, Y.; Kim, H.; Yang, J.; Shin, S. W.; Um, S. H.; Lee, S.; Kang, M. S.; Cho, J. H. Proton-Conductor-Gated MoS₂ Transistors with Room Temperature Electron Mobility of >100 cm² V⁻¹ s⁻¹. *Chemistry of Materials* **2018**, *30*(14), 4527-4535. DOI: 10.1021/acs.chemmater.8b00568.

(47) Ratan, A.; Kunchakara, S.; Dutt, M.; Tripathi, A.; Singh, V. 100 MeV Silicon⁹⁺ swift heavy ion irradiation - Strategic defect annealing approach to enhance the electrical conductivity of few-layered MoS₂ sheets - PVA nanocomposite film. *Vacuum* **2019**, *169*, 108939. DOI: <https://doi.org/10.1016/j.vacuum.2019.108939>.

(48) Salehzadeh, O.; Tran, N. H.; Liu, X.; Shih, I.; Mi, Z. Exciton kinetics, quantum efficiency, and efficiency droop of monolayer MoS₂ light-emitting devices. *Nano Lett* **2014**, *14*(7), 4125-4130. DOI: 10.1021/nl5017283 From NLM PubMed-not-MEDLINE.

(49) He, K.; Kumar, N.; Zhao, L.; Wang, Z.; Mak, K. F.; Zhao, H.; Shan, J. Tightly Bound Excitons in Monolayer WSe_2 . *Physical Review Letters* **2014**, *113*(2), 026803. DOI: 10.1103/PhysRevLett.113.026803.

(50) Cheng, G.; Li, B.; Zhao, C.; Jin, Z.; Li, H.; Lau, K. M.; Wang, J. Exciton aggregation induced photoluminescence enhancement of monolayer WS₂. *Applied Physics Letters* **2019**, *114*(23), 232101. DOI: 10.1063/1.5096206.

(51) Ugeda, M. M.; Bradley, A. J.; Shi, S.-F.; da Jornada, F. H.; Zhang, Y.; Qiu, D. Y.; Ruan, W.; Mo, S.-K.; Hussain, Z.; Shen, Z.-X.; et al. Giant bandgap renormalization and excitonic effects in a monolayer transition metal dichalcogenide semiconductor. *Nature Materials* **2014**, *13*(12), 1091-1095. DOI: 10.1038/nmat4061.

(52) Huo, N.; Yang, Y.; Wu, Y. N.; Zhang, X. G.; Pantelides, S. T.; Konstantatos, G. High carrier mobility in monolayer CVD-grown MoS₂ through phonon suppression. *Nanoscale* **2018**, *10*(31), 15071-15077. DOI: 10.1039/c8nr04416c From NLM PubMed-not-MEDLINE.

(53) Kumar, N.; Cui, Q.; Ceballos, F.; He, D.; Wang, Y.; Zhao, H. Exciton diffusion in monolayer and bulk MoSe₂. *Nanoscale* **2014**, *6*(9), 4915-4919, 10.1039/C3NR06863C. DOI: 10.1039/C3NR06863C.

(54) Rawat, A.; Jena, N.; Dimple; De Sarkar, A. A comprehensive study on carrier mobility and artificial photosynthetic properties in group VI B transition metal dichalcogenide monolayers. *Journal of Materials Chemistry A* **2018**, *6*(18), 8693-8704, 10.1039/C8TA01943F. DOI: 10.1039/C8TA01943F.

(55) Cui, Q.; Ceballos, F.; Kumar, N.; Zhao, H. Transient Absorption Microscopy of Monolayer and Bulk WSe₂. *ACS Nano* **2014**, *8*(3), 2970-2976. DOI: 10.1021/nn500277y.

(56) Wong, J.; Jariwala, D.; Tagliabue, G.; Tat, K.; Davoyan, A. R.; Sherrott, M. C.; Atwater, H. A. High Photovoltaic Quantum Efficiency in Ultrathin van der Waals Heterostructures. *ACS Nano* **2017**, *11*

- (7), 7230-7240. DOI: 10.1021/acsnano.7b03148.
- (57) Yang, S.; Cha, J.; Kim, J. C.; Lee, D.; Huh, W.; Kim, Y.; Lee, S. W.; Park, H.-G.; Jeong, H. Y.; Hong, S.; et al. Monolithic Interface Contact Engineering to Boost Optoelectronic Performances of 2D Semiconductor Photovoltaic Heterojunctions. *Nano Letters* **2020**, *20* (4), 2443-2451. DOI: 10.1021/acs.nanolett.9b05162.
- (58) Shanmugam, M.; Durcan, C. A.; Yu, B. Layered semiconductor molybdenum disulfide nanomembrane based Schottky-barrier solar cells. *Nanoscale* **2012**, *4* (23), 7399-7405, 10.1039/C2NR32394J. DOI: 10.1039/C2NR32394J.
- (59) Wi, S.; Kim, H.; Chen, M.; Nam, H.; Guo, L. J.; Meyhofer, E.; Liang, X. Enhancement of Photovoltaic Response in Multilayer MoS₂ Induced by Plasma Doping. *ACS Nano* **2014**, *8* (5), 5270-5281. DOI: 10.1021/nn5013429.
- (60) Lin, S Nazif, K.; Daus, A.; Hong, J.; Lee, N.; Vaziri, S.; Kumar, A.; Nitta, F.; Chen, M. E.; Kananian, S.; Islam, R.; et al. High-specific-power flexible transition metal dichalcogenide solar cells. *Nat Commun* **2021**, *12* (1), 7034. DOI: 10.1038/s41467-021-27195-7 From NLM PubMed-not-MEDLINE.
- (61) Ulaganathan, R. K.; Yadav, K.; Sankar, R.; Chou, F. C.; Chen, Y.-T. Hybrid InSe Nanosheets and MoS₂ Quantum Dots for High-Performance Broadband Photodetectors and Photovoltaic Cells. *Advanced Materials Interfaces* **2019**, *6*(2), 1801336. DOI: <https://doi.org/10.1002/admi.201801336>.
- (62) Chen, Z.; Liu, H.; Chen, X.; Chu, G.; Chu, S.; Zhang, H. Wafer-Size and Single-Crystal MoSe₂ Atomically Thin Films Grown on GaN Substrate for Light Emission and Harvesting. *ACS Applied Materials & Interfaces* **2016**, *8* (31), 20267-20273. DOI: 10.1021/acsmi.6b04768.
- (63) Tsai, M.-L.; Li, M.-Y.; Retamal, J. R. D.; Lam, K.-T.; Lin, Y.-C.; Suenaga, K.; Chen, L.-J.; Liang, G.; Li, L.-J.; He, J.-H. Single Atomically Sharp Lateral Monolayer p-n Heterojunction Solar Cells with Extraordinarily High Power Conversion Efficiency. *Advanced Materials* **2017**, *29*(32), 1701168. DOI: <https://doi.org/10.1002/adma.201701168>.
- (64) Kwak, D.-H.; Ra, H.-S.; Jeong, M.-H.; Lee, A.-Y.; Lee, J.-S. High-Performance Photovoltaic Effect with Electrically Balanced Charge Carriers in Black Phosphorus and WS₂ Heterojunction. *Advanced Materials Interfaces* **2018**, *5* (18), 1800671. DOI: <https://doi.org/10.1002/admi.201800671>.
- (65) Went, C. M.; Wong, J.; Jahelka, P. R.; Kelzenberg, M.; Biswas, S.; Hunt, M. S.; Carbone, A.; Atwater, H. A. A new metal transfer process for van der Waals contacts to vertical Schottky-junction transition metal dichalcogenide photovoltaics. *Science Advances* **2019**, *5* (12), eaax6061. DOI: doi:10.1126/sciadv.aax6061.
- (66) Fontana, M.; Deppe, T.; Boyd, A. K.; Rinzan, M.; Liu, A. Y.; Paranjape, M.; Barbara, P. Electron-hole transport and photovoltaic effect in gated MoS₂ Schottky junctions. *Scientific Reports* **2013**, *3* (1), 1634. DOI: 10.1038/srep01634.
- (67) Svatek, S. A.; Bueno-Blanco, C.; Lin, D.-Y.; Kerfoot, J.; Macías, C.; Zehender, M. H.; Tobías, I.; García-Linares, P.; Taniguchi, T.; Watanabe, K.; et al. High open-circuit voltage in transition metal dichalcogenide solar cells. *Nano Energy* **2021**, *79*, 105427. DOI: <https://doi.org/10.1016/j.nanoen.2020.105427>.
- (68) Villegas, C. E. P.; Rocha, A. R. Elucidating the Optical Properties of Novel Heterolayered Materials Based on MoTe₂-InN for Photovoltaic Applications. *The Journal of Physical Chemistry C* **2015**, *119* (21), 11886-11895. DOI: 10.1021/jp5122596.
- (69) Kim, K. H.; Andreev, M.; Choi, S.; Shim, J.; Ahn, H.; Lynch, J.; Lee, T.; Lee, J.; Nazif, K. N.; Kumar,

- A.; et al. High-Efficiency WSe₂ Photovoltaic Devices with Electron-Selective Contacts. *ACS Nano* **2022**. DOI: 10.1021/acsnano.1c10054 From NLM Publisher.
- (70) Wang, H.; Wang, W.; Zhong, Y.; Li, D.; Li, Z.; Xu, X.; Song, X.; Chen, Y.; Huang, P.; Mei, A.; et al. Approaching the External Quantum Efficiency Limit in 2D Photovoltaic Devices. *Advanced Materials* **2022**, *34* (39), 2206122. DOI: <https://doi.org/10.1002/adma.202206122>.
- (71) Gupta, A.; Parikh, V.; Compaan, A. D. High efficiency ultra-thin sputtered CdTe solar cells. *Solar Energy Materials and Solar Cells* **2006**, *90* (15), 2263-2271. DOI: <https://doi.org/10.1016/j.solmat.2006.02.029>.
- (72) Chen, H.-L.; Cattoni, A.; De Lépinau, R.; Walker, A. W.; Höhn, O.; Lackner, D.; Siefer, G.; Faustini, M.; Vandamme, N.; Goffard, J.; et al. A 19.9%-efficient ultrathin solar cell based on a 205-nm-thick GaAs absorber and a silver nanostructured back mirror. *Nature Energy* **2019**, *4* (9), 761-767. DOI: 10.1038/s41560-019-0434-y.
- (73) Kaltenbrunner, M.; Adam, G.; Głowacki, E. D.; Drack, M.; Schwödiauer, R.; Leonat, L.; Apaydin, D. H.; Groiss, H.; Scharber, M. C.; White, M. S.; et al. Flexible high power-per-weight perovskite solar cells with chromium oxide-metal contacts for improved stability in air. *Nature Materials* **2015**, *14* (10), 1032-1039. DOI: 10.1038/nmat4388.
- (74) Xue, M.; Nazif, K. N.; Lyu, Z.; Jiang, J.; Lu, C.-Y.; Lee, N.; Zang, K.; Chen, Y.; Zheng, T.; Kamins, T. I.; et al. Free-standing 2.7 μm thick ultrathin crystalline silicon solar cell with efficiency above 12.0%. *Nano Energy* **2020**, *70*, 104466. DOI: <https://doi.org/10.1016/j.nanoen.2020.104466>.
- (75) Xiong, S.; Fukuda, K.; Lee, S.; Nakano, K.; Dong, X.; Yokota, T.; Tajima, K.; Zhou, Y.; Someya, T. Ultrathin and Efficient Organic Photovoltaics with Enhanced Air Stability by Suppression of Zinc Element Diffusion. *Advanced Science* **2022**, *9* (8), 2105288. DOI: <https://doi.org/10.1002/advs.202105288>.
- (76) Pettersson, L. A. A.; Roman, L. S.; Inganäs, O. Modeling photocurrent action spectra of photovoltaic devices based on organic thin films. *Journal of Applied Physics* **1999**, *86* (1), 487-496. DOI: 10.1063/1.370757.
- (77) Hsu, C.; Frisenda, R.; Schmidt, R.; Arora, A.; de Vasconcellos, S. M.; Bratschitsch, R.; van der Zant, H. S. J.; Castellanos-Gomez, A. Thickness-Dependent Refractive Index of 1L, 2L, and 3L MoS₂, MoSe₂, WS₂, and WSe₂. *Advanced Optical Materials* **2019**, *7* (13), 1900239. DOI: <https://doi.org/10.1002/adom.201900239>.
- (78) McPeak, K. M.; Jayanti, S. V.; Kress, S. J. P.; Meyer, S.; Iotti, S.; Rossinelli, A.; Norris, D. J. Plasmonic Films Can Easily Be Better: Rules and Recipes. *ACS Photonics* **2015**, *2* (3), 326-333. DOI: 10.1021/ph5004237.
- (79) National Renewable Energy Laboratory. *Reference Air Mass 1.5 Spectra*. 1962. <https://www.nrel.gov/grid/solar-resource/spectra-am1.5.html> (accessed Dec 2, 2022).
- (80) Ruhstaller, B.; Beierlein, T.; Riel, H.; Karg, S.; Scott, J. C.; Riess, W. Simulating electronic and optical processes in multilayer organic light-emitting devices. *IEEE Journal of Selected Topics in Quantum Electronics* **2003**, *9* (3), 723-731. DOI: 10.1109/JSTQE.2003.818852.
- (81) Ruhstaller, B.; Carter, S. A.; Barth, S.; Riel, H.; Riess, W.; Scott, J. C. Transient and steady-state behavior of space charges in multilayer organic light-emitting diodes. *Journal of Applied Physics* **2001**, *89* (8), 4575-4586. DOI: 10.1063/1.1352027.

Supporting Information

How Good Can 2D Excitonic Solar Cells Be?

Zekun Hu,¹ Da Lin,² Jason Lynch,¹ Kevin Xu,¹ Deep Jariwala^{1,*}

*¹Department of Electrical and Systems Engineering, University of Pennsylvania, Philadelphia, PA,
19104, USA*

*²Department of Materials Science and Engineering, University of Pennsylvania, Philadelphia, PA,
19104, USA*

*Corresponding Author (D.J.) email: dmj@seas.upenn.edu

Section 1. Supplementary figures

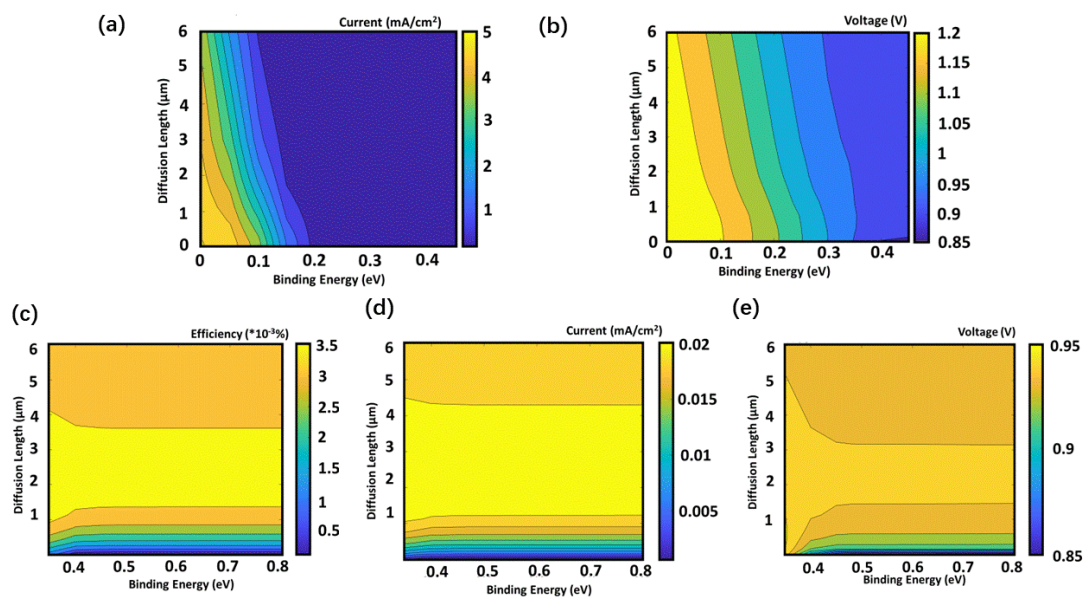


Figure S1. (a) The short-circuit current for the variation of exciton binding energy (0-0.5eV) and diffusion length (0.015-6 μm). (b) The open-circuit voltage for the variation of exciton binding energy (0-0.5eV) and diffusion length (0.015-6 μm). (c) The PCE for the variation of exciton binding energy (0.3-0.8eV) and diffusion length (0.015-6 μm). (d) The short-circuit current for the variation of exciton binding energy (0.3-0.8eV) and diffusion length (0.015-6 μm). (e) The open-circuit voltage for the variation of exciton binding energy (0.3-0.8eV) and diffusion length (0.015-6 μm). (f) The open-circuit voltage for the variation of exciton radiative lifetime (0.1ps-50ns) and exciton non-radiative lifetime (0.1ps-50ns).

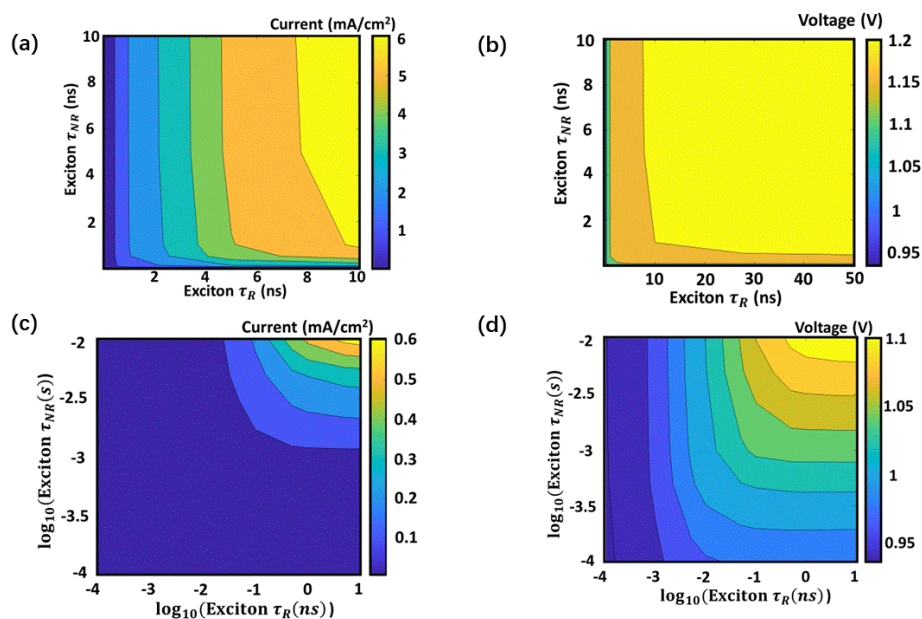


Figure S2. (a) The short-circuit current for the variation of exciton radiative lifetime

(0.1ps-10ns) and exciton non-radiative lifetime (0.1ps-10ns). (b) The open-circuit voltage for the variation of exciton radiative lifetime (0.1ps-50ns) and exciton non-radiative lifetime (0.1ps-10ns). (c) The short-circuit current for the variation of exciton radiative lifetime (0.1ps-10ns) and exciton non-radiative lifetime (0.1ps-10ps). (d) The open-circuit voltage for the variation of exciton radiative lifetime (0.1ps-10ns) and exciton non-radiative lifetime (0.1ps-10ps).

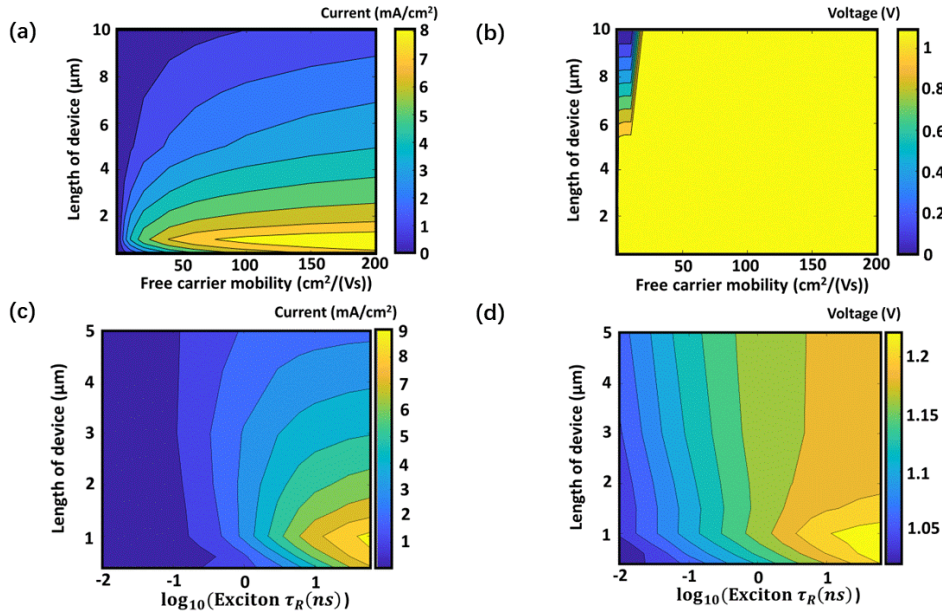


Figure S3. (a) The short-circuit current for the variation of length of device (0.4-10 μm) and free carrier mobility (0.1-200 cm²/(Vs)) under exciton lifetime of 10 ns. (b) The open-circuit voltage for the variation of length of device (0.4-10 μm) and free carrier mobility (0.1-200 cm²/(Vs)) under exciton lifetime of 10 ns. (c) The short-circuit current for the variation of length of device (0.2-10 μm) and exciton lifetime (0.01-6 ns) under free carrier mobility of 60 cm²/(Vs)). (d) The open-circuit voltage for the variation of length of device (0.2-10 μm) and exciton lifetime (0.01-6 ns) under free carrier mobility of 60 cm²/(Vs)).

Section 2. Supplementary tables

Table S1. Detailed Model of simulations

Default MoS ₂ active layer	value
Acceptor Concentration	1E-19 cm ⁻³
Donor Concentration	1E-19 cm ⁻³
Effective Intrinsic Density	1.3E4 cm ⁻³
Electron Affinity	4.723 eV
Temperature	300K
Radiative Recombination (highest)	1.841 cm ⁻³ s ⁻¹
Auger Recombination (highest)	7.489E24 cm ⁻³ s ⁻¹
SRH Recombination (highest)	6.986E22 cm ⁻³ s ⁻¹
Total Recombination (highest)	7.674E24 cm ⁻³ s ⁻¹
Electron Lifetime	1.5E-9 s
Hole Lifetime	1.5E-9 s

Table S2. Tables of parameters in simulations of Figure 2a-b & Figure S1a-e

	value
Material	MoS ₂
Bandgap (eV)	1.8 ¹
Binding energy (eV)	0-0.8
Diffusion length (microns)	0.015-6
Exciton_tau_rad (ns)	0.022 ^{2, 3}
Excitom_Tau_nonrad (ns)	0.002 ^{3, 4}
Free carrier SRH lifetime (s)	1.50E-09 ⁵
Free carrier mobility(cm ² /Vs)	60 ⁶
Device length (microns)	1

Table S3. Tables of parameters in simulations of Figure 2c-d & Figure S2a-d

	value
Material	MoS ₂
Bandgap (eV)	1.8 ¹
Binding energy (eV)	0.24
Diffusion length (microns)	1.5
Exciton_tau_rad (ns)	0.0001-10
Excitom_Tau_nonrad (ns)	0.0001-10
Free carrier SRH lifetime (s)	1.50E-09 ⁵
Free carrier mobility(cm ² /Vs)	60 ⁶

Device length (microns)	1
-------------------------	---

Table S4. Tables of parameters in simulations of Figure 3a-b & Figure S3a-b

	value
Material	MoS ₂
Bandgap (eV)	1.8 ¹
Binding energy (eV)	0.24
Diffusion length (microns)	1.5
Exciton_tau_rad (ns)	0.0001-10
Excitom_Tau_nonrad (ns)	0.0001-10
Free carrier SRH lifetime (s)	1.50E-09 ⁵
Free carrier mobility(cm ² /Vs)	60 ⁶
Device length (microns)	1

Table S5. Tables of parameters in simulations of Figure 3c & Figure S3c-d

	value
Material	MoS ₂
Bandgap (eV)	1.8 ¹
Binding energy (eV)	0.24
Diffusion length (microns)	1.5
Exciton_tau_rad (ns)	0.02-12
Excitom_Tau_nonrad (ns)	0.02-12
Free carrier SRH lifetime (s)	1.50E-09 ⁵
Free carrier mobility(cm ² /Vs)	60 ⁶
Device length (microns)	0.4-5

Table S6. Tables of parameters in simulations of Figure 3d

	value
Material	MoS ₂
Bandgap (eV)	1.8 ¹
Binding energy (eV)	0.24
Diffusion length (microns)	1.5
Exciton_tau_rad (ns)	20
Excitom_Tau_nonrad (ns)	20
Free carrier SRH lifetime (s)	1.50E-09 ⁵
Free carrier mobility(cm ² /Vs)	60 ⁶

Device length (microns)	1
-------------------------	---

Table S7 Tables of detailed input of different materials

Material	MoS ₂	MoSe ₂	WS ₂	WSe ₂
Bandgap (eV)	1.8 ¹	1.6 ⁷	2.04 ⁸	1.65 ⁷
Binding Energy (eV)	0.24 ⁹	0.57 ¹⁰	0.32 ¹¹	0.37 ⁷
Excitons Diffusion length (microns)	1.5 ¹²	0.4 ¹³	0.35 ¹⁴	0.16 ¹⁵
Exciton_tau_rad (ns)	8 ¹²	0.8 ¹⁶	4.4 ¹⁶	3.5 ¹⁶
Free carrier mobility(cm ² /Vs)	60 ⁶	480 ¹³	1060 ¹⁷	250 ¹⁵
Free Carrier Lifetime (ns)	10 ¹⁸	130 ¹³	22 ¹⁴	18 ¹⁵

Section 3. Detailed 3D to 2D convergence simulation.

The simulation was based on a 2D model converged from the 3D model, shown in Figure S4. Initially, a 3D model with larger mesh size was built. Since the third direction duplicates the same structure for times without variation, it has no influence on final results. As shown in Figure S5, different depths tested by the same 3D model show a same PCE. In this case, the 2D simulation with a default depth of 1 micron can correctly represent the 3D model for any depths.

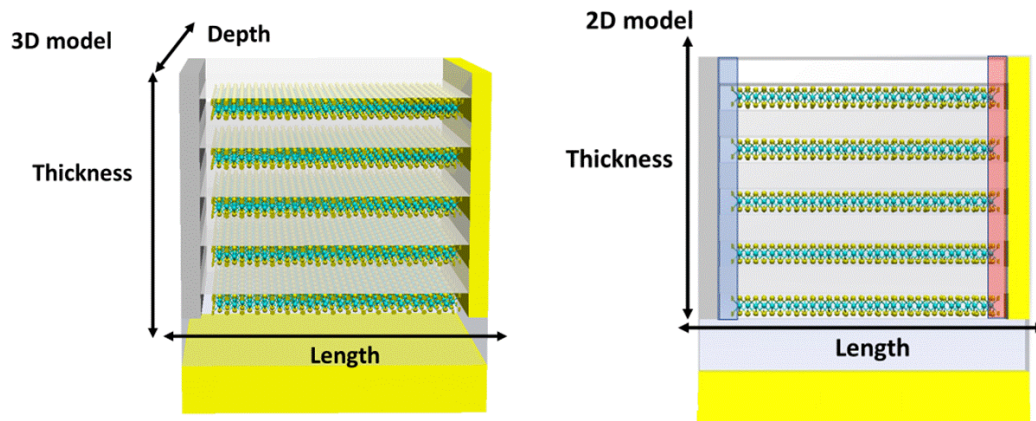


Figure S4. 3D model and 2D model with labelled dimensions.

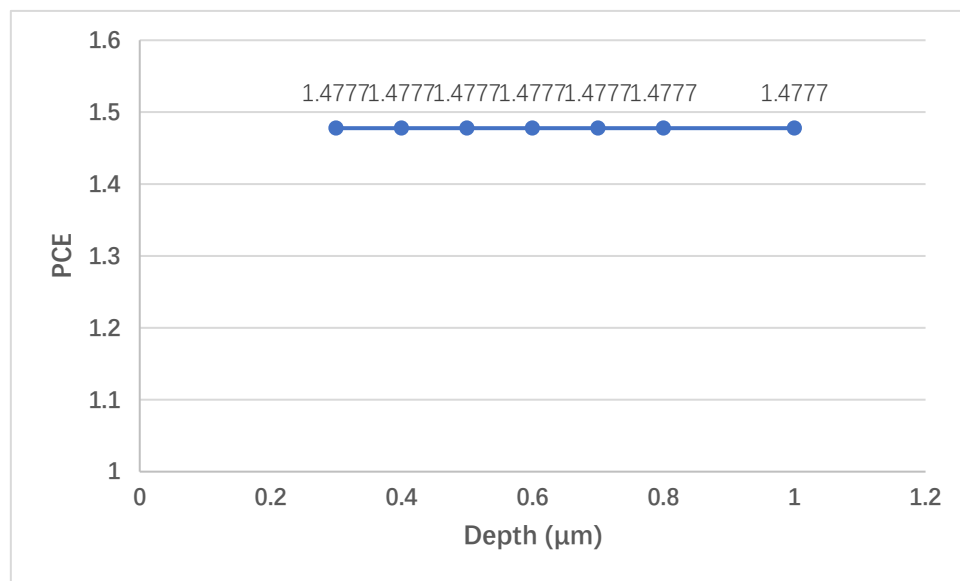


Figure S5. Power conversion efficiency for different depths of the structure in 3D simulations.

The 3D model with a larger mesh size can run a single simulation in an hour. However, as further investigation in Figure S6 shows the results of large mesh size are not reliable. If a smaller mesh size can affect the final results, the current mesh size cannot correctly accurately represent the case. To find a suitable mesh size of the 3D model, a number of simulations was used with smaller mesh sizes. The small mesh size means longer simulation time and heavier computation demand. As we proved the results were not affected by the depth, for some of the small mesh volume, we had to decrease the depth from 1 μm to 0.1 μm . Still, the simulation of the smallest mesh volume of $2.5\text{E-}12 \mu\text{m}^3$ took more than 24 hours to finish and reached the software tolerance of maximum vertices.

Table S8 Tables of 3D simulation

Length h (μm)	Depth (μm)	Thickness (μm)	Length mesh (μm)	Depth mesh (μm)	Thickness mesh (μm)	mesh volume(μm^3)	PCE
1	1	0.0185	0.002	0.002	0.0005	$2.00\text{E-}09$	1.28%
1	1	0.0185	0.001	0.001	0.0005	$5\text{E-}10$	1.88%
1	1	0.0185	0.0005	0.0005	0.00025	$6.25\text{E-}11$	3.79%
1	0.1	0.0185	0.0002	0.0002	0.00005	$2\text{E-}12$	6.22%
1	0.1	0.0185	0.001	0.0001	$2.5\text{E-}05$	$2.5\text{E-}12$	6.27%

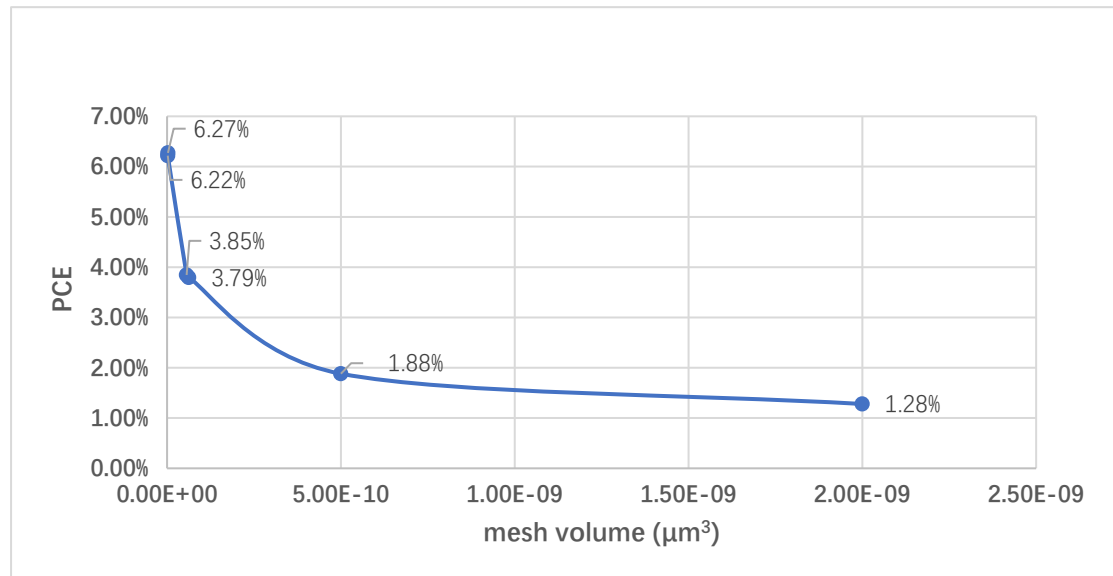


Figure S6. Power conversion efficiency for different mesh volume in 3D simulations.

As the 3D model was not effective to achieve the simulation task, a 2D simulation model was built in Sentaurus. In this software, the default 2D simulation worked as a 3D model with a constant depth of 1 μm , where the depth was not shown on the output. The mesh size of 2D model was optimized to 0.001 μm in length and 0.000025 μm in thickness. As the 0.0185 μm of active layers and insulators was small comparing to the length, a refined mesh size was applied in the direction of thickness. When comparing

the 3D simulation and the 2D simulation under the same condition, the 3D simulation with relatively larger mesh lose PCE of 0.2% due to its mesh in the direction of length, shown in Table S9. Even though we did not have exactly same results for both 2D and 3D simulations, the 2D simulation model converged from 3D simulation was valid.

Table S9 Comparison of 2D simulation and 3D simulation with smallest mesh size

	Length mesh (μm)	Depth mesh (μm)	Thickness mesh (μm)	PCE
3D simulation	0.01	0.001	0.000025	6.38%
2D simulation	0.001	/	0.000025	6.58%

References:

- (1) Castellanos-Gomez, A.; Barkelid, M.; Goossens, A. M.; Calado, V. E.; van der Zant, H. S.; Steele, G. A. Laser-thinning of MoS₂: on demand generation of a single-layer semiconductor. *Nano Lett* **2012**, *12* (6), 3187-3192. DOI: 10.1021/nl301164v From NLM Medline.
- (2) Hong, H.; Cheng, Y.; Wu, C.; Huang, C.; Liu, C.; Yu, W.; Zhou, X.; Ma, C.; Wang, J.; Zhang, Z.; et al. Modulation of carrier lifetime in MoS₂ monolayer by uniaxial strain*. *Chinese Physics B* **2020**, *29* (7). DOI: 10.1088/1674-1056/ab99ba.
- (3) Wang, H.; Zhang, C.; Chan, W.; Manolatu, C.; Tiwari, S.; Rana, F. Radiative lifetimes of excitons and trions in monolayers of the metal dichalcogenide MoS₂. *Physical Review B* **2016**, *93* (4). DOI: 10.1103/PhysRevB.93.045407.
- (4) Palummo, M.; Bernardi, M.; Grossman, J. C. Exciton radiative lifetimes in two-dimensional transition metal dichalcogenides. *Nano Lett* **2015**, *15* (5), 2794-2800. DOI: 10.1021/nl503799t From NLM Medline.
- (5) He, J.; Fang, W. H.; Long, R.; Prezhdo, O. V. Superoxide/Peroxide Chemistry Extends Charge Carriers' Lifetime but Undermines Chemical Stability of CH₃NH₃PbI₃ Exposed to Oxygen: Time-Domain ab Initio Analysis. *J Am Chem Soc* **2019**, *141* (14), 5798-5807. DOI: 10.1021/jacs.8b13392 From NLM PubMed-not-MEDLINE.
- (6) Huo, N.; Yang, Y.; Wu, Y. N.; Zhang, X. G.; Pantelides, S. T.; Konstantatos, G. High carrier mobility in monolayer CVD-grown MoS₂ through phonon suppression. *Nanoscale* **2018**, *10* (31), 15071-15077. DOI: 10.1039/c8nr04416c From NLM PubMed-not-MEDLINE.
- (7) He, K.; Kumar, N.; Zhao, L.; Wang, Z.; Mak, K. F.; Zhao, H.; Shan, J. Tightly Bound Excitons in Monolayer WSe_2 . *Physical Review Letters* **2014**, *113* (2), 026803. DOI: 10.1103/PhysRevLett.113.026803.
- (8) Cheng, G.; Li, B.; Zhao, C.; Jin, Z.; Li, H.; Lau, K. M.; Wang, J. Exciton aggregation induced photoluminescence enhancement of monolayer WS₂. *Applied Physics Letters* **2019**, *114* (23), 232101. DOI: 10.1063/1.5096206.
- (9) Park, S.; Mutz, N.; Schultz, T.; Blumstengel, S.; Han, A.; Aljarb, A.; Li, L.-J.; List-Kratochvil, E. J. W.; Amsalem, P.; Koch, N. Direct determination of monolayer MoS₂ and WSe₂ exciton binding energies on insulating and metallic substrates. *2D Materials* **2018**, *5* (2), 025003. DOI: 10.1088/2053-1583/aaa4ca.
- (10) Ugeda, M. M.; Bradley, A. J.; Shi, S.-F.; da Jornada, F. H.; Zhang, Y.; Qiu, D. Y.; Ruan, W.; Mo, S.-K.; Hussain, Z.; Shen, Z.-X.; et al. Giant bandgap renormalization and excitonic effects in a monolayer transition metal dichalcogenide semiconductor. *Nature Materials* **2014**, *13* (12), 1091-1095. DOI: 10.1038/nmat4061.
- (11) Hill, H. M.; Rigosi, A. F.; Roquelet, C.; Chernikov, A.; Berkelbach, T. C.; Reichman, D. R.; Hybertsen, M. S.; Brus, L. E.; Heinz, T. F. Observation of Excitonic Rydberg States in Monolayer MoS₂ and WS₂ by Photoluminescence Excitation Spectroscopy. *Nano Letters* **2015**, *15* (5), 2992-2997. DOI: 10.1021/nl504868p.
- (12) Uddin, S. Z.; Kim, H.; Lorenzon, M.; Yeh, M.; Lien, D.-H.; Barnard, E. S.; Htoon, H.; Weber-Bargioni, A.; Javey, A. Neutral Exciton Diffusion in Monolayer MoS₂. *ACS Nano* **2020**, *14* (10), 13433-13440. DOI: 10.1021/acsnano.0c05305.
- (13) Kumar, N.; Cui, Q.; Ceballos, F.; He, D.; Wang, Y.; Zhao, H. Exciton diffusion in monolayer and bulk MoSe₂. *Nanoscale* **2014**, *6* (9), 4915-4919, 10.1039/C3NR06863C. DOI: 10.1039/C3NR06863C.

- (14) He, J.; He, D.; Wang, Y.; Cui, Q.; Ceballos, F.; Zhao, H. Spatiotemporal dynamics of excitons in monolayer and bulk WS₂. *Nanoscale* **2015**, *7* (21), 9526-9531, 10.1039/C5NR00188A. DOI: 10.1039/C5NR00188A.
- (15) Cui, Q.; Ceballos, F.; Kumar, N.; Zhao, H. Transient Absorption Microscopy of Monolayer and Bulk WSe₂. *ACS Nano* **2014**, *8* (3), 2970-2976. DOI: 10.1021/nn500277y.
- (16) Palummo, M.; Bernardi, M.; Grossman, J. C. Exciton Radiative Lifetimes in Two-Dimensional Transition Metal Dichalcogenides. *Nano Letters* **2015**, *15* (5), 2794-2800. DOI: 10.1021/nl503799t.
- (17) Rawat, A.; Jena, N.; Dimple; De Sarkar, A. A comprehensive study on carrier mobility and artificial photosynthetic properties in group VI B transition metal dichalcogenide monolayers. *Journal of Materials Chemistry A* **2018**, *6* (18), 8693-8704, 10.1039/C8TA01943F. DOI: 10.1039/C8TA01943F.
- (18) Uddin, S. Z.; Kim, H.; Lorenzon, M.; Yeh, M.; Lien, D. H.; Barnard, E. S.; Htoon, H.; Weber-Bargioni, A.; Javey, A. Neutral Exciton Diffusion in Monolayer MoS₂. *ACS Nano* **2020**, *14* (10), 13433-13440. DOI: 10.1021/acsnano.0c05305 From NLM PubMed-not-MEDLINE.